Switchable ionic selectivity of membranes with electrically conductive surface: Theory and experiment

Ilya I. Ryzhkov [a,b,*], Margarita A. Shchurkina [b], Elena V. Mikhlina [a], Mikhail M. Simunin [b], Ivan V. Nemtsev [b,c]

[a] *Institute of Computational Modelling SB RAS, Akademgorodok 50–44, Krasnoyarsk 660036, Russia*
[b] *Siberian Federal University, Svobodny 79, Krasnoyarsk 660041, Russia*
[c] *Federal Research Center KSC SB RAS, Akademgorodok 50, Krasnoyarsk 660036, Russia*

ARTICLE INFO

ABSTRACT

Nanoporous membranes with electrically conductive surface represent an important class of stimuli–responsive materials. The variation of surface potential provides a powerful tool for adjusting ionic selectivity, conductivity, and rejection. This work is devoted to the theoretical and experimental study of switchable ionic selectivity. The one–dimensional Space charge (SC) and two–dimensional Uniform potential (UP) models are first generalized to constant surface potential case taking into account the Stern layer with inner (iHp) and outer (oHp) Helmholtz planes. The ionic selectivity is investigated experimentally by measuring the membrane potential at zero current for C–Nafen membranes prepared from alumina nanofibers with conductive carbon coating. The evolution of charging current is used to determine the dependence of surface charge density and differential capacitance on the applied potential. These data are fitted by the UP and SC models to find the Stern layer capacitance. It is shown that the variation of surface potential results in a continuous change of ionic selectivity from anion to cation. The membrane potential data are fitted by the UP and SC models using the chemical charge density and concentration boundary layer thickness as fitting parameters. It allows to determine the potential, at which the membrane becomes non–selective. The SC and UP models provide close results for membrane potential and surface charge density and demonstrate a good agreement with the experimental data. The UP model overestimates the solution velocity and ion concentrations at the membrane surface, while it underestimates the ion fluxes and iHp/oHp potentials. This work essentially extends our understanding of ion transport in stimuli–responsive membranes operated by the electric field. The results can be applied in the area of nanofiltration, (reverse) electrodialysis, electrochemical sensors, and nanofluidic devices.

© 2021 Elsevier Ltd. All rights reserved.

1. Introduction

An increasingly important and rapidly developing area of modern membrane science is represented by stimuli–responsive, or smart gating membranes [1]. The selectivity and permeability of such membranes can be altered and adjusted in response to environmental signals, such as changes in temperature, ionic strength, pH, light, electric and magnetic fields, and chemical cues [2]. The smart membranes are designed by chemically / physically incorporating stimuli–responsive materials such as polymer layers or metal coatings into porous membrane substrates, or introducing these materials directly during membrane formation [3–5]. Due to a large variety of gating strategies and fabrication techniques, stimuli–responsive membranes find a wide range of applications in chemical separation and purification [6], water treatment [7], controlled drug delivery [8], chemical and bio–sensors [9] as well as synthetic analogues of biological ion channels and pumps [10,11].

Over the last two decades, a lot of research has been focused on the development of nanochannel systems and nanoporous membranes, which can change their transport properties in ionic solutions in response to the applied electric field [12]. When the channel dimensions become comparable to the Debye length, the direct manipulation of ion transport through the nanochannel can be performed by applying a transmembrane potential difference and/or varying the surface charge [13]. If membrane material is electrically conductive, then the surface charge can be altered by applying a prescribed potential to the membrane. It provides a powerful tool for changing and adjusting such membrane characteristics as ionic selectivity, ionic conductivity, and ion rejection.

* Corresponding author at: Institute of Computational Modelling SB RAS, Federal Research Center KSC SB RAS, Akademgorodok 50–44, 660036 Krasnoyarsk, Russia.
E-mail address: rii@icm.krasn.ru (I.I. Ryzhkov).

The possibility of switching the ionic selectivity from cation to anion by varying the surface potential was first demonstrated using track–etched membranes modified by electroless plating of gold on the pore walls [14,15]. Later, it was shown that the diffusion fluxes of anionic and cationic permeate species can be varied as a function of applied electrical potential [16]. However, a disadvantage of modified track–etched membranes is very low porosity, which prevents their use in filtration applications. A mesoporous carbon–based membrane, which can regulate the transport of organic dye molecules by changing the applied surface potential, was suggested in [17]. Using layered graphene–based membranes with sub 2–nm pores, the authors of [18] showed that ion diffusion rates can be reversibly modulated and anomalously enhanced by externally varying the surface potential. The principle of electrostatic gating was also employed for modulation of ionic selectivity in a single nanopore [19] and control of ionic conduction in field–effect reconfigurable ionic diodes [20]. A significant enhancement of ionic conductivity of a porous matrix [21] and a gold nanotube membrane [22] was demonstrated by varying the applied surface potential. However, it was found that this effect can be screened by adsorption of electrolyte ions on the pore surface. A nanoporous gold membrane, which allowed selective permeation of small molecule analytes via tuning the charge of self–assembled monolayer by changing the pH or surface potential, was described in [23]. A composite nanofiltration membrane based on a conducting polymer and carbon nanotubes was first proposed in [24]. An enhancement in the rejection of monovalent ions was shown by increasing the applied surface potential without affecting membrane permeability. The different rejection rates of chloride and sulfate anions in graphene oxide membranes placed in an electric field were found in [25].

The first attempts to theoretically describe ion transport in conductive membranes were based on a number of essential simplifications. The authors of [26] employed the Nernst–Planck flux equation and replaced constant surface potential with constant volume charge density in order to explain the experimental results [14,15] on switchable ionic selectivity. The impact of pH and ionic strength on ion transport through gold nanotubule membranes was theoretically investigated in [27]. Analyzing the experimental data on tunable ion transport [15], the authors of [28] assumed equal salt concentrations in the reservoirs separated by the membrane although they were different in the experiment. These studies provided only satisfactory (qualitative) agreement with the experiment. The molecular dynamics was employed for studying the electrically tunable ion selectivity in charged graphene nanopores [29].

One of the common approaches to describe membranes is based on capillary models, where the membrane is represented as an array of cylindrical pores. The classical two–dimensional Space charge (SC) model [30] and its one–dimensional analogue known as Uniform potential (UP) model [31] were developed for nanopores with constant surface charge density. These models were revisited and simplified computationally in [32], and their extension to allow for fluid slip was suggested in [33]. The models were applied to the analysis of electrokinetic phenomena [34], determination of zeta potential [35], membrane potential and membrane conductivity [36,37], as well as to the studies of electrokinetic energy conversion [38]. The Space charge model was first generalized to the case of constant surface potential in [39]. A comparison between ion transport in nanofiltration membranes with constant surface charge / potential was performed in [40]. A new effect of enhancing the membrane potential at zero current due to the induced charge [41,42] on the conductive surface was discovered in [43,44]. However, the calculations based on the SC model [45] showed that the range of surface potentials, within which the membrane selectivity changes from cation to anion, is

an order of magnitude lower than in the experiment [15]. It was shown that the agreement between theory and experiment can be improved by taking into account the Stern layer [46]. Further modification of the model to include the presence of both electronic and pH–dependent chemical charge on the pore surface was proposed in [47]. It was based on the previously developed theory of amphifunctional interfaces allowing both electronic and ionic surface charging processes [48,49]. The model of electrified interface, which takes into account the chemisorption of oxygen species on a metal surface and a layer of oriented water molecules was proposed in [50]. It was shown that the model predicts non–monotonic dependence of surface charge on the surface potential for a water–filled Pt nanopore [51,52].

The literature overview shows that electric field responsive membranes are actively being developed, but their use in membrane processes faces a number of challenges: the choice of material for selective layer and substrate, electrochemical stability, interaction of ions with conductive surface, selectivity and permeability in binary and multi–ionic solutions. From the theoretical side, a major challenge is the development of mathematical models, which can adequately describe the ion transport in nanopores with simultaneous presence of electronic and ionic surface charge.

This work is devoted to the theoretical and experimental study of switchable ionic selectivity in conductive membranes. We provide the first generalization of Uniform potential (UP) and Space charge (SC) models to constant surface potential case taking into account the Stern layer with inner and outer Helmholtz planes in the presence of chemical charge. The models are validated against experimental results for C–Nafen membranes prepared from alumina nanofibers with conductive carbon coating [53–55]. The latter are the first ceramic membranes, which allow electric field–responsive ion transport, while the previous studies [15,17,24,25] were focused on different types of polymeric membranes.

2. Theoretical part

2.1. Main configuration

Consider a porous membrane of thickness L_p, which separates two reservoirs denoted by L (left) and R (right). They are kept at pressures P_L and P_R and electrical potentials Φ_L and Φ_R, respectively. The reservoirs contain aqueous solutions of the same monovalent and symmetric (1:1) electrolyte with concentrations C_L and C_R, respectively. The membrane surface is electrically conductive and has the potential Φ_e. We are interested in the case, where the ion transport is generated by the concentration difference between reservoirs ($C_L \geqslant C_R$) and applied electric current I in the absence of pressure difference ($P_L = P_R = 0$). The potential difference $\Delta\Phi = \Phi_R - \Phi_L$ between reservoirs results from the Donnan potential jumps at the membrane/solution interfaces, the diffusion potential induced by the difference of ion diffusion coefficients, and the applied electric current. It can be assumed without loss of generality that $\Phi_L = 0$. The membrane potential for an ideally selective membrane is given by Tanaka [56]

$$\Delta\Phi_I^{\pm} = \pm \frac{R_g T}{F} \ln \frac{C_L}{C_R}, \tag{1}$$

where the plus or minus signs correspond to the membrane, which transports only cations or only anions, respectively. At high electrolyte concentration, the activities should be used instead of concentrations in formula (1).

The values of electrical potential, ion concentrations, and pressure, which are specified in the reservoirs, should be maintained just near the membrane surface. However, the diffusion of electrolyte through the membrane can result in the appearance of con-
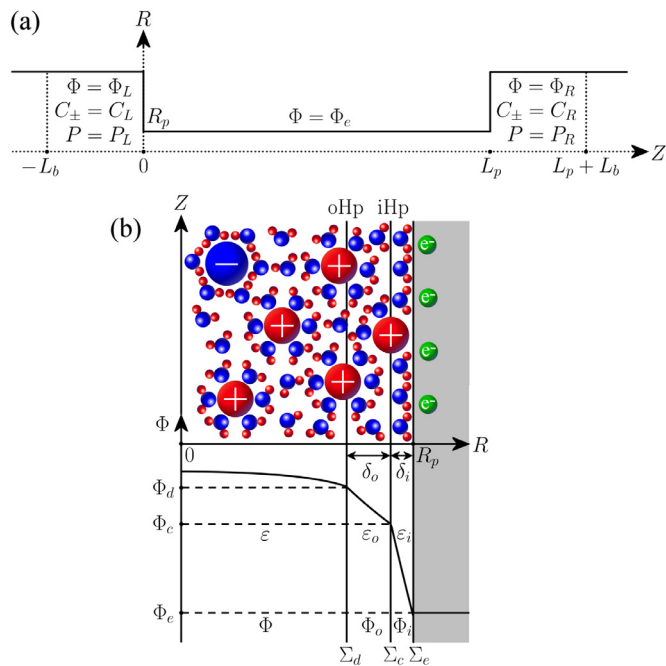
(a)

(b)

Fig. 1. A cylindrical nanopore connecting two reservoirs (a). The scheme of electric double layer model in the nanopore (b).

centration boundary layers of thickness L_b, which cause the increase (decrease) of concentration near the membrane from the low (high) concentration side, respectively [57,58]. In this case, the specified values of all quantities should be maintained at a distance of L_b from the membrane surface.

A membrane is modelled as an array of cylindrical pores of length L_p and radius R_p, where the cylindrical coordinates R in radial and Z in axial directions are introduced, see Fig. 1 (a). Thus, it is enough to calculate the distribution of potential, ion concentrations, and pressure in a single pore and adjacent boundary layers if they are taken into account.

2.2. The electric double layer model

The Gouy–Chapman–Stern model [48,49,59,60] is used for describing the electric double layer (EDL) in the nanopore. The scheme of EDL model is shown in Fig. 1 (b). The charge at the conductive pore wall is formed by electrons, which can be injected or withdrawn with the help of external power source. The potential Φ_e of the pore wall is constant. On the contrary, the electronic charge density Σ_e is not constant, but varies along the pore to compensate the non–uniform potential distribution in the pore interior and ensure that the pore wall is an equipotential surface [39,41,47].

The solution side of the EDL is divided into the diffuse layer and the Stern layer, which in turn consists of two parts. The inner part of thickness δ_i and relative permittivity ε_i contains the water molecules oriented by the near–wall electric field. It is bounded by the inner Helmholtz plane (iHp), where the partially desolvated and specifically adsorbed ions as well as ionic charges arising from chemically reactive surface groups are located. The chemical charge density and electrical potential at the iHp are denoted by Σ_c and Φ_c, respectively. The outer part of the Stern layer with the thickness δ_o and relative permittivity ε_o is bounded by the outer Helmholtz plane (oHp) also known as the surface of closest approach for ions in solution. The potential at the oHp is denoted by Φ_d. We assume that there is no ionic charge present directly at the oHp. However, we can define the surface charge density Σ_d, which

should be placed at the oHp to balance the ionic charge in the diffuse layer. This quantity will be discussed further in Section 2.3. Note that the inner and outer parts of the Stern layer contain only water molecules and are assumed to be charge–free. Due to the orientation of water molecules in these layers, their relative permittivities typically obey the relation $\varepsilon_i \leqslant \varepsilon_o \leqslant \varepsilon$, where ε is the relative permittivity of the diffuse layer [59]. This layer extends from the oHp to the pore axis, where it can overlap with the diffuse layer from the opposite wall if the pore radius is comparable with or smaller than the Debye length. The described EDL model is consistent with recent experimental studies of EDL structure by the X–ray photoelectron spectroscopy [61].

2.3. The Stern layer model

Since there are no ions in the inner and outer parts of the Stern layer, the electrical potentials $\Phi_i(R, Z)$ and $\Phi_o(R, Z)$ inside them satisfy the Laplace equation, which becomes one–dimensional when the derivatives with respect to Z are neglected within the approximation of a long cylindrical pore ($L_p \gg R_p$) [32]. This equation is readily solved taking into account the potential values Φ_e at the pore surface, $\Phi_c(Z)$ at the iHp, and $\Phi_d(Z)$ at the oHp:

$$\Phi_i = \Phi_e + \frac{\Phi_c(Z) - \Phi_e}{\ln\left(1 - \frac{\delta_i}{R_p}\right)} \ln\left(\frac{R}{R_p}\right),$$

$$\Phi_o = \Phi_c(Z) + \frac{\Phi_d(Z) - \Phi_c(Z)}{\ln\left(1 - \frac{\delta_o}{R_p - \delta_i}\right)} \ln\left(\frac{R}{R_p - \delta_i}\right). \tag{2}$$

The boundary conditions for electric field should be satisfied at the inner Helmholtz plane

$$-\varepsilon_i \varepsilon_0 \frac{\partial \Phi_i}{\partial R}(R_p - \delta_i, Z) = -\varepsilon_o \varepsilon_0 \frac{\partial \Phi_o}{\partial R}(R_p - \delta_i, Z) + \Sigma_c \tag{3}$$

and at the outer Helmholtz plane

$$-\varepsilon_o \varepsilon_0 \frac{\partial \Phi_o}{\partial R}(R_p - \delta_i - \delta_o, Z) = -\varepsilon \varepsilon_0 \frac{\partial \Phi}{\partial R}(R_p - \delta_i - \delta_o, Z). \tag{4}$$

Here $\Phi(R, Z)$ is the potential in the diffuse layer, and ε_0 is the vacuum permittivity. The chemical charge density Σ_c in (3) can in general depend on the local concentration of ions, which is in turn related to the local value of potential. If, for example, the protonation / deprotonation reactions occur at the pore surface, the chemical charge is determined by the local pH of the solution [50–52,62]. In this work, we consider the simplest case of constant Σ_c. The electronic charge is determined by

$$\Sigma_e(Z) = \varepsilon_i \varepsilon_0 \frac{\partial \Phi_i}{\partial R}(R_p, Z), \tag{5}$$

while the charge density and potential at the diffuse layer boundary (oHp) are given by

$$\Sigma_d(Z) = \varepsilon \varepsilon_0 \frac{\partial \Phi}{\partial R}(R_p - \delta_i - \delta_o, Z), \qquad \Phi_d(Z) = \Phi(R_p - \delta_i - \delta_o, Z). \tag{6}$$

Consider a cylindrical pore section with the radius $R'_p = R_p - \delta_i - \delta_o$ located between Z and $Z + \Delta Z$. It can be shown using the Gauss theorem and Eq. (6) that $\Sigma_d(Z)$ is equal in magnitude and opposite in sign to the diffuse layer charge in this section divided by its surface area when $\Delta Z \to 0$ and the approximation $L_p \gg R'_p$ is valid. So, $\Sigma_d(Z)$ is the local charge density, which should be placed at the oHp in order to balance the local diffuse layer charge. To simplify the notation, the Z dependence of Φ_c, Φ_d and Σ_e, Σ_d will not be stated hereafter.

Now we substitute solutions (2) into boundary conditions (3) and (4) taking into account (6). It allows to obtain the relation between the charge density Σ_d and potential Φ_d as well as to

express the potential Φ_c at the iHp via the above quantities:

$$\Sigma_d = C_s(\Phi_e - \Phi_d) + \Sigma_c', \tag{7}$$

$$\Phi_c = \frac{\Sigma_d}{C_o} + \Phi_d, \tag{8}$$

where

$$C_s = \left(\frac{1}{C_i} \frac{R_p - \delta_i - \delta_o}{R_p - \delta_i} + \frac{1}{C_o} \right)^{-1}, \qquad \Sigma_c' = \frac{C_s}{C_i} \Sigma_c. \tag{9}$$

The quantity Σ_c' is the effective chemical charge, which is induced at the oHp due to the presence of chemical charge Σ_c at the iHp, while C_s is the total Stern layer capacitance. The latter is determined by the capacitances C_i and C_o of the inner and outer parts, respectively:

$$C_i = \frac{\varepsilon_i \varepsilon_0}{(R_p - \delta_i) \ln\left(\frac{R_p}{R_p - \delta_i} \right)},$$

$$C_o = \frac{\varepsilon_o \varepsilon_0}{(R_p - \delta_i - \delta_o) \ln\left(\frac{R_p - \delta_i}{R_p - \delta_i - \delta_o} \right)}. \tag{10}$$

It should be noted that the detailed information about the Stern layer structure (relative permittivities and thicknesses of inner and outer parts) is not always available from the experiments. At the same time, the (differential) capacitance of a porous electrode can be accurately measured and used for prediction of Stern layer characteristics [63]. Thus, a simplification of the above–described model can be suggested by considering a Stern layer, which extends from the pore surface to the diffuse layer boundary (oHp) and has the thickness $\delta_s = \delta_i + \delta_o$, relative permittivity ε_s, and the corresponding capacitance given by

$$C_s = \frac{\varepsilon_s \varepsilon_0}{(R_p - \delta_s) \ln\left(\frac{R_p}{R_p - \delta_s} \right)}. \tag{11}$$

The relation between surface potential Φ_e and diffuse layer potential Φ_d in this case coincides with (7) assuming that the effective chemical charge Σ_c' is present at the diffuse layer boundary.

In what follows, we will need the values of potential and charge density averaged over the pore surface as well inner and outer Helmholtz planes. The average electronic charge density is defined by

$$\overline{\Sigma}_e = \frac{1}{2\pi R_p L_p} \int_0^{L_p} \int_0^{2\pi} \Sigma_e R_p \, d\Phi \, dZ. \tag{12}$$

The average potentials $\overline{\Phi}_c$ and $\overline{\Phi}_d$ as well as average chemical charge density $\overline{\Sigma}_c$ and oHp charge density $\overline{\Sigma}_d$ are defined similarly to (12), where one should replace R_p with $R_p - \delta_i$ for iHp and with $R_p - \delta_i - \delta_o$ for oHp.

2.4. The Space charge model of the diffuse layer

When the pore radius is larger than the Debye length, the variations of potential, ion concentrations, and pressure in radial direction of the pore should be taken into account. In this case, the two–dimensional Space charge (SC) model should be used for describing the diffuse layer. This model was derived from the Navier–Stokes, Nernst–Planck, and Poisson equations for constant surface charge density at the pore wall [30,32], and recently adapted for the case of constant surface potential [39]. In this work, we first propose the generalization of the Space charge model to the case when the presence of Stern layer leads to the relation between the surface charge density and surface potential according to Eq. (7).

The transport of electrolyte in the diffuse layer of the nanopore is characterized by the solution velocity $\boldsymbol{U} = (U, V)$, pressure P,

cation C_+ and anion C_- concentrations (mol/m³), and electrical potential Φ, which are functions of axial and radial coordinates. The ions in the nanopore are transported by convection, diffusion, and migration in the electric field. The fluxes of ions are written as

$$\boldsymbol{J}_\pm = C_\pm \boldsymbol{U} - D_\pm \nabla C_\pm \mp \frac{D_\pm F}{R_g T} C_\pm \nabla \Phi,$$

where $D_\pm$ are the ion diffusion coefficients, R_g is the ideal gas constant, T is the temperature, and F is the Faraday constant.

Let us introduce dimensionless variables by

$$R = R_p' r, \qquad Z = L_p z, \qquad \boldsymbol{U} = \frac{D_-}{L_p} \boldsymbol{u}, \qquad P = C_* R_g T \, p,$$

$$C_\pm = C_* c_\pm, \qquad \Phi = \frac{R_g T}{F} \varphi, \qquad \boldsymbol{J}_\pm = \frac{D_- C_*}{L_p} \boldsymbol{j}_\pm,$$

where $R_p' = R_p - \delta_i - \delta_o$ is the radius corresponding to the location of outer Helmholtz plane, C_* is the reference concentration taken as 1 mol/m³, and $\boldsymbol{u} = (u, v)$. The dimensionless potentials and surface charge densities at the pore wall, inner and outer Helmholtz planes are introduced according to

$$\Phi_e = \frac{R_g T}{F} \varphi_e, \qquad \Phi_c = \frac{R_g T}{F} \varphi_c, \qquad \Phi_d = \frac{R_g T}{F} \varphi_d,$$

$$\Sigma_e = \frac{\varepsilon \varepsilon_0 R_g T}{F R_p} \sigma_e, \quad \Sigma_c = \frac{\varepsilon \varepsilon_0 R_g T}{F(R_p - \delta_i)} \sigma_c, \quad \Sigma_d = \frac{\varepsilon \varepsilon_0 R_g T}{F(R_p - \delta_i - \delta_o)} \sigma_d. \tag{13}$$

In what follows, we will need the quantities averaged over the part of pore cross–section, which contains the diffuse layer. The dimensional average axial velocity is defined by

$$\overline{V} = \frac{2}{R_p'^2} \int_0^{R_p'} V R \, dR.$$

The average pressure $\overline{P}$, ion concentrations $\overline{C}_\pm$, potential $\overline{\Phi}$, axial ion fluxes $\overline{J}_\pm$, total axial ion flux $\overline{J} = \overline{J}_+ + \overline{J}_-$, and axial charge flux $\overline{I} = \overline{J}_+ - \overline{J}_-$ are introduced in the same way. The corresponding dimensionless quantities are $\overline{v}$, $\overline{p}$, $\overline{c}_\pm$, $\overline{\varphi}$, $\overline{j}_\pm$, $\overline{j} = \overline{j}_+ + \overline{j}_-$, and $\overline{i} = \overline{j}_+ - \overline{j}_-$. Note that the charge flux is related to the applied current density I (A/m²) by the formula $\overline{I} = I/F$.

In the SC model, the dimensionless potential φ, ion concentrations $c_\pm$, and pressure p are represented as [32]

$$\varphi(r, z) = \phi_v(z) + \psi(r, z), \quad c_\pm(r, z) = c_v(z) \exp(\mp\psi(r, z)), \tag{14}$$

$$p(r, z) = p_v(z) + 2c_v(z) \cosh(\psi(r, z)),$$

where $\phi_v(z)$, $c_v(z)$, $p_v(z)$ are the virtual potential, concentration, and pressure, respectively. The function ψ satisfies the Poisson equation with boundary condition of axial symmetry

$$\frac{1}{r} \frac{\partial}{\partial r} \left(r \frac{\partial \psi(r, z)}{\partial r} \right) = \frac{c_v(z)}{\lambda^2} \sinh \psi(r, z), \tag{15}$$

$$\frac{\partial \psi}{\partial r}(0, z) = 0. \tag{16}$$

Here $\lambda = \sqrt{\varepsilon \varepsilon_0 R_g T / 2F^2 C_*}/R_p'$ is the dimensionless Debye length. The boundary condition at $r = 1$ is derived from relation (7) at the oHp taking into account (6), (10) and (13):

$$\psi(1, z) + (\mu + v) \frac{\partial \psi}{\partial r}(1, z) = \varphi_e - \phi_v(z) + \mu\sigma_c, \tag{17}$$

where

$$\mu = \frac{\varepsilon}{\varepsilon_i} \ln\left(\frac{R_p}{R_p - \delta_i} \right), \qquad v = \frac{\varepsilon}{\varepsilon_o} \ln\left(\frac{R_p - \delta_i}{R_p - \delta_i - \delta_o} \right). \tag{18}$$

When the simplified model based on a single Stern layer is used, one should put $\delta_o = 0$ (i.e. $v = 0$) and formally replace δ_i with δ_s and ε_i with ε_s in (18) as well as σ_c with σ_c' in (17), where

σ'_c is the dimensionless analogue of Σ'_c. If the Stern layer is not considered at all ($\delta_i = \delta_o = 0$), then it follows from (17) that

$$\psi(1, z) = \varphi_e - \phi_v(z).$$

This is the boundary condition for constant surface potential case previously derived in [43].

Now let us derive the expression for dimensionless potential φ_c at the iHp. It follows from (6), (13), and (14) that

$$\sigma_d(z) = \frac{\partial \psi}{\partial r}(1, z), \qquad \phi_d(z) = \phi_v(z) + \psi(1, z). \tag{19}$$

Using these relations, we obtain from (8)

$$\varphi_c(z) = \nu \sigma_d(z) + \varphi_d(z).$$

The dimensionless electronic charge can be determined from (5) taking into account solutions (2), boundary conditions (3), (4), and relations (6), (13):

$$\sigma_e(z) = \sigma_d(z) - \sigma_c. \tag{20}$$

Note that σ_d is equal in magnitude and opposite in sign to the local diffuse layer charge density. Then Eq. (20) can be represented as the charge balance relation $\sigma_e + \sigma_c + (-\sigma_d) = 0$.

Let us define the potential, at which the average charge density at the oHp is zero. This quantity is useful since the ion transport through the nanopore is mainly determined by the charge on the diffuse layer boundary. By averaging the first formula in (19) and boundary condition (17) over the pore surface and putting $\overline{\sigma}_d = 0$, we find

$$\varphi_e = -\mu \overline{\sigma}_c + \int_0^1 (\phi_v(z) + \psi(1, z)) \, dz. \tag{21}$$

The dimensional analogue of (21) is given by

$$\Phi_{\overline{\Sigma}_d = 0} = -\frac{\overline{\Sigma}_c}{C_i} + \overline{\Phi}_d. \tag{22}$$

This equation shows that $\Phi_{\overline{\Sigma}_d = 0}$ can be shifted to positive or negative direction by changing the chemical charge density in negative or positive direction, respectively.

Now we can proceed with the formulation of Space charge model working equations. The relation of the average volume flux $\overline{v}$ (or average axial velocity), average ion flux $\overline{j} = \overline{j}_+ + \overline{j}_-$, and average charge flux $\overline{i} = \overline{j}_+ - \overline{j}_-$ to the gradients of virtual pressure p_v, virtual chemical potential $\mu_v = \ln c_v$, and virtual electrical potential ϕ_v can be written in the form of phenomenological flux–force formalism [32]:

$$\left(\frac{dp_v}{dz}, \frac{d\mu_v}{dz}, \frac{d\phi_v}{dz}\right)^T = L\left(\overline{v}, \overline{j}, \overline{i}\right)^T. \tag{23}$$

Here $L = -\mathcal{L}^{-1}$ is the symmetric 3×3 matrix. The coefficients of matrix $\mathcal{L} = \{\mathcal{L}_{ij}(z)\}$ depend on the function $\psi(r, z)$ and virtual concentration $c_v(z)$. They are given in Section 1 of the Supplementary Data.

The boundary conditions for Eq. (23) are derived by putting $\psi(r, z) = 0$ in (14) and taking into account the dimensional values of potential, ion concentration, and pressure in the reservoirs (see Section 2.1 and Fig. 1 (a)):

$$\begin{aligned} z = 0: \quad & p_v = p_L - 2c_L, \quad c_v = c_L, \quad \phi_v = \varphi_L, \\ z = 1: \quad & p_v = p_R - 2c_R, \quad c_v = c_R, \quad \phi_v = \varphi_R. \end{aligned} \tag{24}$$

When the ion transport is driven by the concentration difference between the reservoirs and the applied electric current, the dimensionless charge flux $\overline{i}$ is known and the potential φ_R should be determined. It can be also assumed without loss of generality that $\varphi_L = 0$. If there is no pressure gradient, one should also put $p_L = p_R = 0$.

We have proposed a new numerical algorithm for solving the SC model equations. It is described in Section 1 of the Supplementary Data.

2.5. The Uniform potential model of the diffuse layer

When the nanopore radius is comparable with or less than the Debye length, the profiles of potential, ion concentrations, and pressure in the radial direction become almost uniform. In this case, one can neglect the radial dependence of all quantities. This approach is known as the Uniform potential (UP) model [32].

We start with the description of charge density at the diffuse layer boundary (oHp) in the form (7), where $\Phi_d = \Phi(Z)$ is the potential distribution in the pore, which is uniform at each cross–section of $Z = \text{const}$. The dimensionless electronic, chemical and diffuse volume charge densities are introduced according to

$$X_e = \frac{2\Sigma_e}{FR_p C_*}, \qquad X_c = \frac{2\Sigma_c}{F(R_p - \delta_i)C_*}, \qquad X = \frac{2\Sigma_d}{F(R_p - \delta_i - \delta_o)C_*}.$$

It follows from (7) and the above definitions that

$$X = c_s(\varphi_e - \varphi) + X'_c, \tag{25}$$

where the dimensionless capacitance c_s and the effective volume chemical charge density X'_c are given by

$$c_s = \frac{2C_s R_g T}{F^2 R'_p C_*}, \qquad X'_c = \frac{R_p - \delta_i}{R'_p} \frac{C_s}{C_i} X_c.$$

The governing equations of UP model are derived from those of SC model taking into account essential simplifications, which arise when the radial dependence of all quantities is ignored [32,47]. Taking into account the expression (25) for volume charge density, these equations can be written as [46]

$$\frac{dp}{dz} = -8\alpha \, \overline{v} + X \frac{d\varphi}{dz}, \tag{26}$$

$$\begin{aligned} \frac{dc}{dz} = \frac{1}{2cD}\Big(&(D+1)\big(c^2 - X^2\big)\overline{v} - \big((D-1)X + (D+1)c\big)\overline{j} \\ &- \big((D+1)X + (D-1)c\big)\overline{i}\Big) - \frac{c_s X}{c}\frac{d\varphi}{dz}, \end{aligned} \tag{27}$$

$$\frac{d\varphi}{dz} = \frac{1}{2D(c + c_s)}\Big(\big((D-1)c - (D+1)X\big)\overline{v} - (D-1)\,\overline{j} - (D+1)\,\overline{i}\Big). \tag{28}$$

Here $c = c_+ + c_-$ is the total concentration of cations and anions. The effective volume charge density X is equal in magnitude and opposite in sing to the ionic charge density

$$X = c_- - c_+. \tag{29}$$

The boundary conditions inside the pore at the inlet from the left reservoir and the outlet to the right reservoir are written as

$$z = 0: \quad p = p_L + c - 2c_L, \quad c = \sqrt{X^2 + 4c_L^2}, \quad \varphi = \varphi_0. \tag{30}$$

$$z = 1: \quad p = p_R + c - 2c_R, \quad c = \sqrt{X^2 + 4c_R^2}, \quad \varphi = \varphi_1. \tag{31}$$

Here, φ_0 and φ_1 are the Donnan potential jumps. The corresponding concentrations and osmotic pressure jumps are described by the first and second conditions in formulas (30) and (31), respectively. Given that $c_\pm = c_L \exp(\mp\varphi_0)$ at $z = 0$ and substituting these relations in (29), we obtain the equation to determine the potential φ_0:

$$c_s(\varphi_e - \varphi_0) + X'_c = 2c_L \sinh(\varphi_0 - \varphi_L). \tag{32}$$

The relation analogues to (32) at $z = 1$ is given by

$$c_s(\varphi_e - \varphi_1) + X'_c = 2c_R \sinh(\varphi_1 - \varphi_R). \tag{33}$$

When the ion transport is driven by the concentration difference and the applied electric current, the resulting dimensionless potential difference can be determined from (33):

$$\Delta\varphi = \varphi_R - \varphi_L = \varphi_1 - \text{arcsinh}\left(\frac{c_s(\varphi_e - \varphi_1) + X_c'}{2c_R}\right) - \varphi_L.$$

The numerical algorithm for solving the UP model equations is described in Section 2 of the Supplementary Data.

The dimensionless potential value, at which the average charge density at the diffuse layer boundary (oHp) is zero, can be determined by averaging Eq. (25) and putting $\overline{X} = 0$:

$$\varphi_e = -\frac{\overline{X}_c'}{c_s} + \int_0^1 \varphi \, dz.$$

This formula is the analogue of relation (21) for the UP model. The corresponding dimensional formula is given by (22).

2.6. The concentration boundary layer model

When concentration boundary layers of thickness L_b near the membrane surface are taken into account, the ion transport within them can be described by system (26)–(28) in the absence of volume charge ($X = 0$, i.e. $c_s = 0$ and $X_c' = 0$):

$$\frac{dp}{dz} = -8\alpha\,\epsilon\,\overline{v},$$
$$\frac{dc}{dz} = \frac{\epsilon}{2D}\left((D+1)c\,\overline{v} - (D+1)\,\overline{j} - (D-1)\,\overline{i}\right), \qquad (34)$$
$$\frac{d\varphi}{dz} = \frac{\epsilon}{2cD}\left((D-1)c\,\overline{v} - (D-1)\,\overline{j} - (D+1)\,\overline{i}\right).$$

Here ϵ is a factor that constricts the flow and represents the fraction of membrane area actually available to solution flow, ion and charge fluxes [57]. When the membrane is modelled as an array of parallel cylindrical pores, ϵ corresponds to the membrane porosity.

To determine the profiles of pressure, ion concentrations, and potential in the left boundary layer (see Fig. 1a), one should impose the boundary conditions

$$z = -l_b: \qquad p = p_L, \qquad c = 2c_L, \qquad \varphi = \varphi_L, \qquad (35)$$

where $l_b = -L_b/L_p$. The integration of Eq. (34) from $z = -l_b$ to $z = 0$ allows one to determine the pressure p_L', ion concentration c_L', and potential φ_L' at the membrane surface $z = 0$. Similarly, the integration of the same system from $z = 1 + l_b$ to $z = 1$ with boundary conditions

$$z = 1 + l_b: \qquad p = p_R, \qquad c = 2c_R, \qquad \varphi = \varphi_R \qquad (36)$$

provides the values p_R', c_R', φ_R' at the membrane surface $z = 1$. The obtained values of all quantities should be used in boundary conditions (24) for the SC model and in boundary conditions (30) and (31) for the UP model. The modification of solution algorithms for taking into account the boundary layers is described in Section 3 of the Supplementary Data.

3. Experimental part

3.1. Membrane preparation

The membranes are produced from Nafen™, which is supplied by ANF Technology in the form of blocks composed of highly aligned γ–phase alumina nanofibers with the diameter of 10–15 nm and length more than 100 mm [64]. Nafen nanofibers are dispersed in deionized water using a magnetic stirrer for 60 minutes (the weight ratio of Nafen:water is 1:200). Then the ultrasonic treatment is applied to the solution for 15 min with 20% amplitude (Sonics & Materials VC–505, USA). The alignment of Nafen fibers facilitates their separation from each other and allows preserving

relatively high aspect ratios ($\sim$100) after treatment. The resulting colloidal solution is filtered through a coarse polytetrafluoroethylene (PTFE) filter (average pore size of 0.6 μm) using a Sartorius AG system and a fore vacuum pump MPC 105 T (ILMVAC GmbH, Germany). At the next stage, the sample is separated from the substrate and dried at 80 °C for 2 h under a load of stainless steel plate. Then the sample is sintered at 300 °C during 4 h, which ensures its structural stability in aqueous solutions. The resulting Nafen membrane is a white circular disk with the diameter of 40 mm and thickness of about 400 μm.

The carbon coating is deposited on the membrane by chemical vapor deposition (CVD). The setup consists of the tube furnace OTF–1500X–UL–3, the liquid vaporization system LVD–F1 (MTI, USA), and the vacuum pump PC 3001 VARIO (Vacuubrand GMBH, Germany). In this work, the ethanol vapour is used as a carbon–containing precursor instead of propane, which was employed previously [53,54]. A sample is placed in the tube furnace and heated with the rate of 5 °C/min in an argon atmosphere at flow rate of 100 mL/min. The deposition is performed at the temperature of 900 °C and pressure of 0.5 bar during 15 min in a mixture of ethanol (95.6 %) – water (4.4 %) vapour at volume flow rate of 0.5 mL/min in the liquid phase and argon at volume flow rate of 2000 mL/min. Then the sample is cooled to 150 °C with the rate of 5 °C/min in an argon atmosphere. When a membrane is subjected to carbon deposition, the preliminary sintering at 300 °C is not required. The samples with and without deposited carbon layer are referred to as C–Nafen membrane and Nafen membrane, respectively.

3.2. Membrane characterization

The morphology of prepared membranes was characterized by the Scanning electron microscopy using FE–SEM Hitachi S–5500 instrument (Japan) operating at 3 kV. Before examination, the membrane samples were coated with platinum by magnetron sputtering during 1 min at the current of 10 mA and the pressure of $8 \cdot 10^{-6}$ Bar in argon atmosphere. The TEM images were obtained by the Hitachi HT7700 instrument (Japan) with an accelerating voltage of 100 kV. The cross–sectional samples for TEM studies were prepared by the focused ion beam instrument Hitachi FB2100 (Japan) operating at 40 kV.

Membrane pore and surface area characterization was performed by low temperature nitrogen adsorption experiments using ASAP–2420 (Micromeritics, USA). Relative pressure (P/P_0) range was 0–0.99, and measure gas was dosed in an incremental mode. The dose increment was 2 cm^3/g for P/P_0 range 0–0.001, while it was 10 cm^3/g for P/P_0 from 0.001 up to 0.995. Equilibration interval was equal to 40 seconds. Nitrogen saturation pressure was measured at every isotherm point to calculate P_0 and analysis bath temperature. Textural characteristics calculations of materials under consideration were realized with the BET model.

Thermal analysis of carbon coated samples was performed on NETZCH Jupiter 449 with mass–spectrometer detector. A sample was crushed with the pestle and mortar. After that, it was placed into Pt melting pot on the differential sensor with identical Pt melting pot as a reference and then heated in the oven unit in the air up to 1200 °C.

3.3. Electrochemical measurements

To study the effect of electric field on the ionic selectivity of C–Nafen membranes, the experimental setup schematically shown in Fig. 2 (a) is developed. It includes the laboratory made electrochemical cell, which consists of two compartments L and R separated by a membrane. The cell body is made of chemically inert polytetrafluoroethylene (PTFE), which allows working with a wide
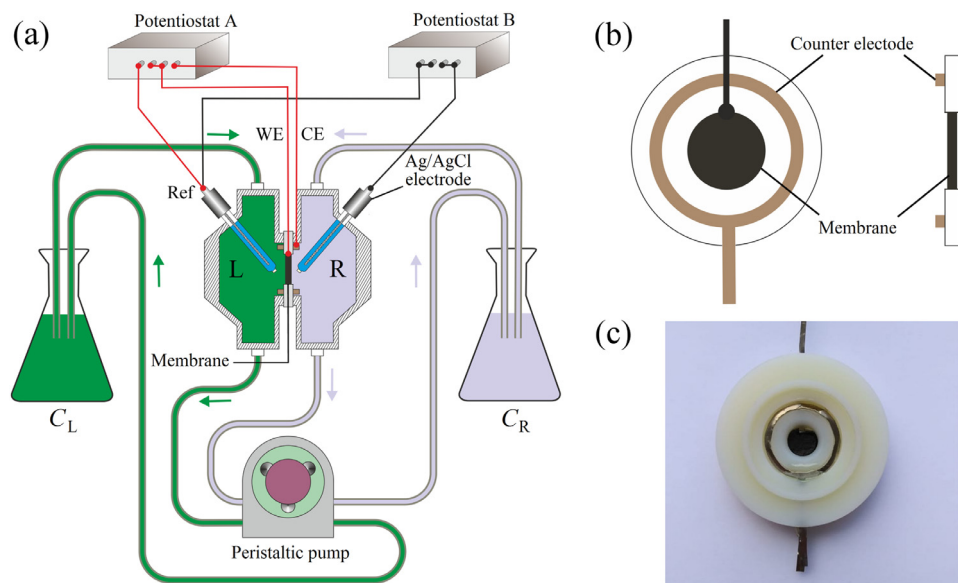
Fig. 2. The scheme of experimental setup for studying switchable ionic selectivity (a), the scheme of membrane holder (b), and the photo of a membrane inside the holder (c).

range of chemicals. The working aqueous solutions are pumped through the compartments by the Lead fluid BT601L peristaltic pump (China) with Masterflex L/S Easy–Load II Head (USA) to maintain the fixed salt concentrations C_L and C_R in them ($C_L \geqslant C_R$). The volume of solution in each compartment is 100 ml, while the flasks shown in Fig. 2 (a) contain 5 L of solution. Such large volume is needed to prevent the change of solution concentration due to slow leakage of electrolyte from the Ag/AgCl 4.2 M electrodes. The pumping flow rate is set to 100 ml/min.

The application of external potential to the membrane is realized with the help of Potentiostat A (P–20X, Electrochemical instruments, Russia), which operates in the three–electrode mode. The working electrode (WE) is the membrane, the counter electrode (CE) is the titanium foil, and the reference electrode (Ref) is the 4.2 M Ag/AgCl. The membrane and two rings of titanium foil are inserted in a specially designed holder made of polyamide nylon 6 (Fig. 2 (b,c)) using an epoxy glue. The platinum wire or activated carbon cloth can also be used instead of titanium foil. The potentiostat A applies a prescribed potential to the membrane with respect to the reference electrode and monitors the charging current until it vanishes.

Potentiostat B (PI–50 Pro, Electrochemical instruments, Russia) operates in the broken circuit potential measurement mode and measures the potential difference between the two compartments (membrane potential at zero current) with the help of 4.2 M Ag/AgCl electrodes. The input impedance of this device is 10^{12} Ω. The potentiostats A and B share the same electrode in the left compartment of the cell. The configuration, where the potentiostat B is connected to a separate (third) reference electrode is also possible. It is used to perform the cyclic voltammetry of electrically conductive C–Nafen membrane.

The measurements are performed in KCl aqueous solutions. Prior to the experiment, the holder with the membrane is kept in a solution with a lower concentration C_R for 12 h at room temperature of 25 °C. Then the membrane is installed into the cell, which is filled with the working solutions of concentrations C_L and C_R. First, the measurement of membrane potential at zero current is performed. After that, a series of prescribed potentials is applied consecutively to the membrane. At each applied potential, the membrane potential is measured until the equilibrium state is reached. The latter is characterized by the vanishing charg-

Table 1
The characteristics of Nafen and C–Nafen membranes.

Membrane	Pore size nm	Specific surface area m²/g	Specific pore volume cm³/g	Porosity
Nafen	33 ± 16	140	0.72	0.74
C–Nafen	26 ± 14	120	0.53	0.65

ing current and the stationary value of membrane potential. Further details on the measurement procedure will be discussed in Section 4.4.

4. Results and discussion

4.1. Membrane morphology and textural properties

The SEM image of Nafen membrane surface in Fig. 3 (a) shows that it consists of randomly oriented alumina nanofibers with the length of 0.5–1 μm. The deposition of carbon leads to thickening of nanofibers and decreasing the space between them, see Fig. 3 (b). The TEM images of membrane slices perpendicular to its surface confirm the formation of several ordered carbon layers on the nanofibers with the total thickness of around 5 nm, see Fig. 3 (c).

The pore size distribution curves are shown in Fig. 3 (d), while the characteristics of Nafen and C–Nafen membranes are presented in Table 1. The average pore size and its standard deviation are calculated from the presented distributions. As expected, the deposition of carbon decreases the specific surface area, pore volume, and membrane porosity. It also shifts the pore size distribution curve in the direction of smaller pore size values and eliminates the micropores (< 2 nm in size). The thermal analysis of carbon coated samples with the synthesis parameters described in Section 3.1 provides the carbon mass fraction of 0.075, which corresponds to the mass gain of 8.1 % after the carbon deposition. Using these data and taking into account the specific pore volume v_p, the density of alumina $\rho_a = 3.89$ g/cm³ and deposited carbon $\rho_c = 1.75$ g/cm³, the porosity of Nafen and C–Nafen membranes can be estimated by the formula [54]

$$\phi = \left(1 + \frac{\rho_c + \alpha \rho_a}{\rho_a \rho_c v_p (1 + \alpha)} \right)^{-1},$$
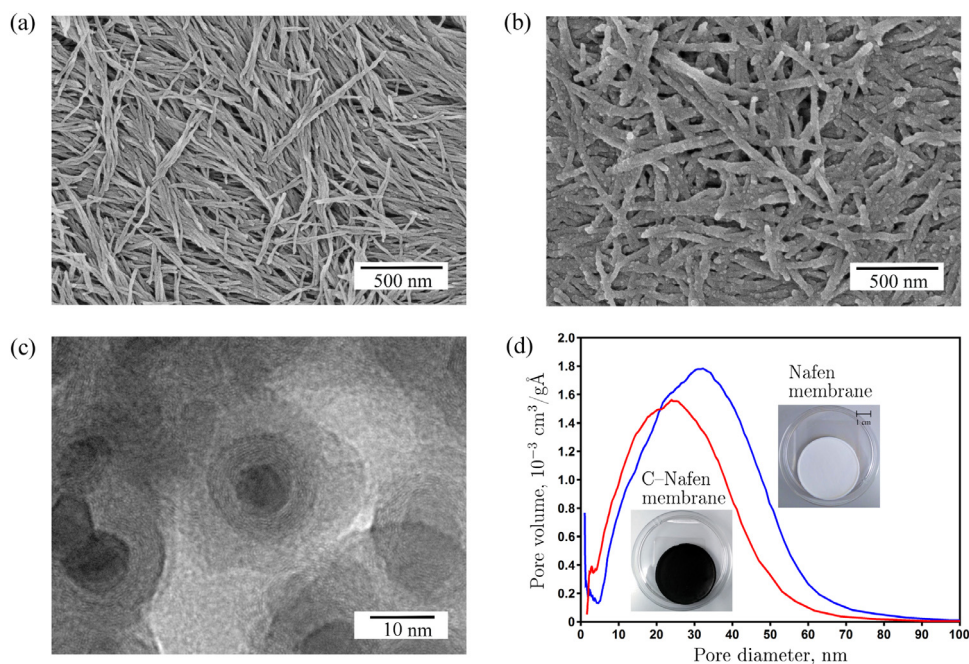
Fig. 3. SEM images of the membrane surface before (a) and after (b) deposition of carbon. TEM image of a part of membrane slice perpendicular to its surface (c). Pore size distribution for Nafen and C–Nafen membranes (d).

where $\alpha = 0.081$ is mass fraction gain after carbon deposition ($\alpha = 0$ for the Nafen membrane). The calculated porosity values given in Table 1 show that the membranes are highly porous. Note that the characteristics of membranes obtained from ethanol precursor are slightly different from those obtained from propane in [65]. Both Nafen and C–Nafen membranes are hydrophilic.

More information about the preparation and characterization of Nafen and C–Nafen membranes (SEM and TEM imaging, thermal analysis, X-ray fluorescent microanalysis, Raman spectroscopy, X–ray photoelectron spectroscopy, electrical resistance measurements) can be found in [53,54,65].

4.2. Model physical parameters

In this section, we describe the values of physical parameters, which correspond to the performed experiments and will be used in theoretical models for fitting the experimental data. The membrane parameters are as follows: the pore length is 400 μm and the pore radius mean value is $R_p = 13$ nm (see Section 3.2). The pore radius standard deviation (7 nm) will be also taken into account in the analysis below. The temperature is fixed at $T = 298.15$ K. The solution viscosity $\mu = 0.888 \cdot 10^{-3}$ Pa·s and relative permittivity $\varepsilon = 78.5$ correspond to water. The diffusion coefficients of potassium and chloride ions are $D_+ = 1.957 \cdot 10^{-9}$ m^2/s and $D_- = 2.032 \cdot 10^{-9}$ m^2/s, respectively. The range of electrolyte concentration is 1 mM – 100 mM, while the applied surface potential varies from −600 mV to +600 mV.

The Stern layer characteristics are based on the recent experimental study using the X–ray photoelectron spectroscopy [61]. The thickness of the inner part is taken as $\delta_i = 0.2$ nm (a single layer of water molecules) and the thickness of the outer part is set to $\delta_o = 0.4$ nm (half of the hydrated ion diameter). Thus, the total Stern layer thickness is $\delta_s = 0.6$ nm.

The calculations on the basis of UP and SC models developed in Section 2 and previous studies using simplified models [46] suggest that the variations of Stern layer permittivities, pore radius, and thickness of boundary layers have a similar effect on the membrane potential dependence on the surface potential. Namely, the

decrease of Stern layer permittivities and increase of pore radius as well as boundary layer thickness reduce the variation of membrane potential with the applied voltage. It corresponds to the reduction of ionic selectivity and more smooth transition between cation and anion selective states. Thus, a reliable determination of all above–described parameters by fitting the experimental data on membrane potential is not possible. At least part of these parameters should be obtained from independent measurements. Note that the pore radius have been already determined from low temperature nitrogen adsorption experiments, see Section 3.2. In the next section, the Stern layer characteristics will be experimentally determined and discussed.

4.3. Electrochemical properties of C–Nafen membrane

We use two methods for electrochemical characterization of C–Nafen membranes: cyclic voltammetry and potentiostatic charging. Both studies are performed using the three–electrode mode, which is realized with the help of Potentiostat A (see the scheme of experimental setup in Fig. 3). The measurements are performed in a 10 mM KCl aqueous solution in both reservoirs separated by the membrane. The mass of membrane sample is 30 mg.

The results of cyclic voltammetry (CVA) with the scan rate of 1 mV/s are presented in Fig. 4. It can be seen that the voltamperogram does not exhibit any oxidation or reduction waves in the range of applied potentials from −600 mV to +600 mV. So, the C–Nafen membrane is close to an ideally polarized electrode in the above potential range. The absence of electrochemical reactions is necessary for potentiostatic control of ion transport through the membrane. The differential capacitance in μF/cm^2 is calculated from the CVA data by the formula

$$C_d = \frac{1}{A}\frac{dQ}{d\Phi_e} = \frac{1}{A}\frac{I dt}{d\Phi_e} = \frac{I}{A\nu}, \tag{37}$$

where Q is surface charge, I is the current, ν is the potential scan rate, and $A = mS$ is the membrane surface area determined from the membrane mass m and specific surface area S (see Table 1). The differential capacitance in F/g can be obtained from formula
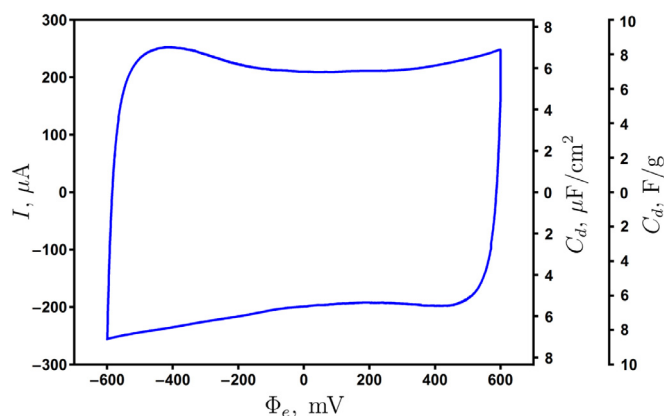
Fig. 4. The cyclic voltammetry of C–Nafen membrane in 10 mM KCl aqueous solution with the scan rate of 1 mV/s.

(37), where the membrane surface area should be replaced by the membrane mass. Note that formula (37) is valid when the product of capacitance and cell resistance is small, so the current quickly attains a steady state value and remains constant during the linear potential sweep [66]. Fig. 4 shows that the current does not change appreciably on the upper and lower branches of CVA. Thus, the differential capacitance of C–Nafen membrane can be estimated as 6 μF/cm^2 or 7 F/g. The capacitance values on the right axes are calculated from the current values on the left axis by formula (37) assuming that $I > 0$ for $\nu > 0$ and $I < 0$ for $\nu < 0$. These conditions correspond to both branches of CVA except very small regions near ± 600 mV.

The potentiostatic charging experiment is performed by successively applying the potentials from +600 mV to −600 mV with the step of 100 mV to the membrane surface with respect to 4.2 M Ag/AgCl electrode. The measured charging current is shown in Fig. 5. Positive current corresponds to the transfer of positive charge from the counter electrode to the working electrode (membrane), while negative current corresponds to the transfer of electrons in the same direction. When no charging is applied, the potential of membrane with respect to 4.2 M Ag/AgCl electrode in 10 mM KCl electrolyte is measured to be around 270 mV. The first application of +600 mV leads to the transfer of positive charge to the membrane, so the current is positive. The successive decrease of surface potential by 100 mV shifts the surface charge in

negative direction by transferring electrons from the counter electrode to the membrane, so the current is negative. At each step, the measurement is performed until the current reaches a constant value. This value is close to zero for positive potentials, so the membrane acts as an ideally polarized electrode. For negative potentials, a small residual current is observed, and its magnitude increases with increasing the magnitude of applied potential. Apparently, this residual current has a faradaic nature and originates from very slow electrochemical reactions between carbon surface groups and aqueous KCl electrolyte. The study of C–Nafen membrane surface by the X–ray photoelectron spectroscopy [65] revealed the presence of C=O, C–OH, and COOH functional groups. However, a detailed analysis of electrochemical surface reactions lies outside the scope of this work. In what follows, we will show that a slight deviation of C–Nafen membrane performance from an ideally polarized electrode does not prevent the potentiostatic control of ionic transport and selectivity for negative applied potentials.

The evolution of charging current with time shown in Fig. 5 allows us to determine the dependence of surface charge and differential capacitance on the applied surface potential. The procedure for calculation of surface charge density Σ_i and differential capacitance C_i, which correspond to the applied potential Φ_i, $i = 1, \ldots, n$ is described in Section 4 of the Supplementary Data. The obtained dependence of differential capacitance on the surface potential of C–Nafen membrane is shown in Fig. 6 (a). The capacitance reaches minimum at $\Phi_e = 0$ mV, which suggests that this value is close to the potential of zero average surface charge [59]. The obtained results are consistent with those obtained from cyclic voltammetry (Fig. 4). The surface charge densities determined from potentiostatic charging are shown in Fig. 6 (b). The dependence of Σ_e on Φ_e is almost linear and crosses the origin.

The differential capacitance can be also determined from the SC and UP models by taking equal concentrations $C_L = C_R = 10$ mM and equal pressures $P_L = P_R = 0$ in the reservoirs. The pore radius is fixed at 13 nm. In the calculations, the potential is varied in the range from −600 mV to +600 mV with the step of $\Delta\Phi_e = 1$ mV. At each step, the change of surface charge density $\Delta\Sigma_e$ is calculated, and differential capacitance is determined by $C_d = \Delta\Sigma_e / \Delta\Phi_e$. The UP and SC models are used to fit the experimental data on differential capacitance with the Stern layer capacitance C_s as a fitting parameter. The corresponding Stern layer relative permittivity can be found from (11) taking into account the Stern layer thickness $\delta_s = 0.6$ nm. The chemical charge is set to zero (non–zero chemical
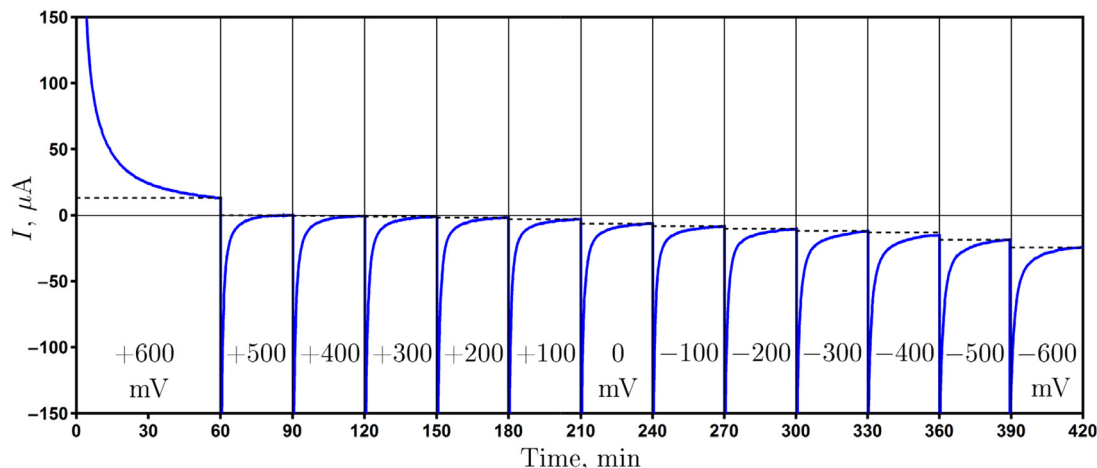

Fig. 5. The charging current vs time for different potentials applied to the surface of C–Nafen membrane in 10 mM KCl aqueous solution. The dashed lines show the level of residual current.
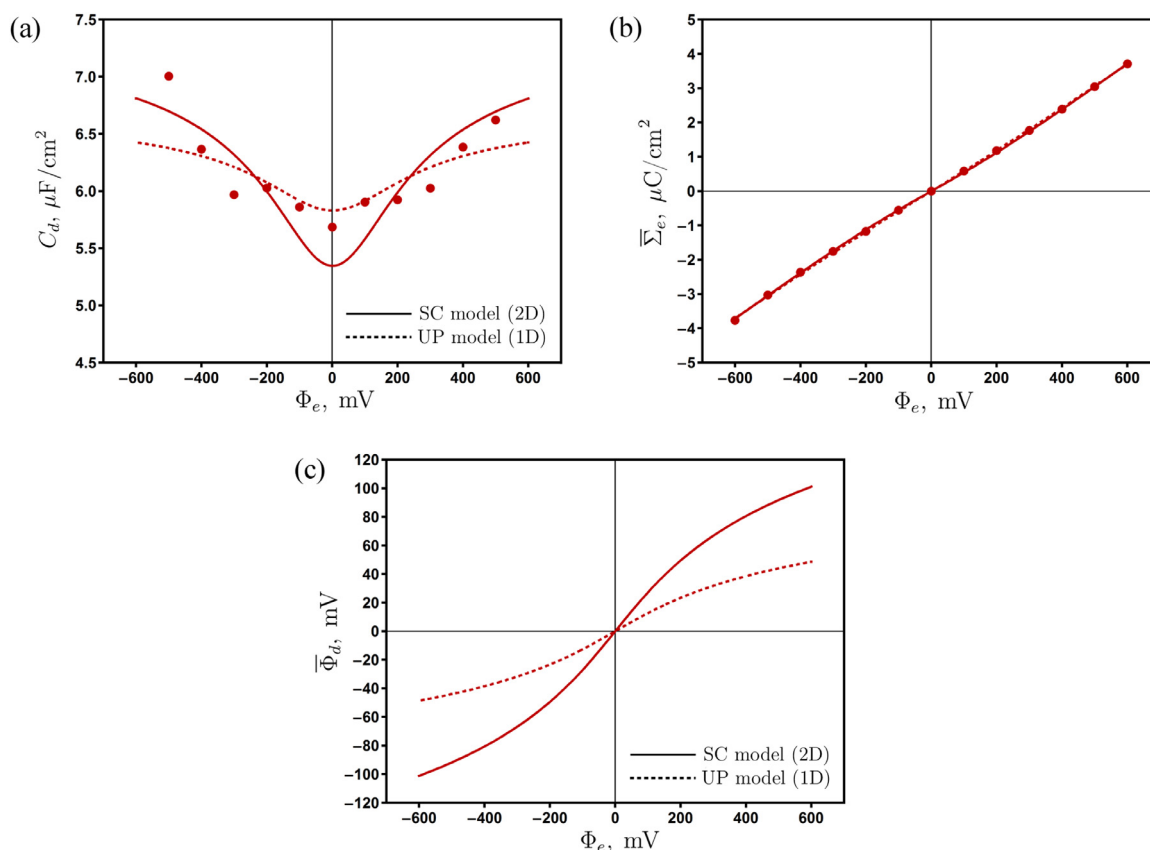
Fig. 6. The differential capacitance (a), average surface charge density (b), and average diffuse layer potential (c) for C–Nafen membrane in 10 mM KCl aqueous solution. Experiment (circles), fitting of experimental data by the SC model (solid curves) and by the UP model (dashed curves).

Table 2
The Stern layer properties. The capacitance C_s is fitted from the experimental data on membrane differential capacitance.

Model	Stern layer			Inner part			Outer part		
	δ_s nm	ε_s	C_s μF/cm^2	δ_i nm	ε_i	C_i μF/cm^2	δ_o nm	ε_o	C_o μF/cm^2
UP model	0.6	4.66	7.04	0.2	2.0	8.9	0.4	13.3	29.9
					3.0	13.4		6.4	14.4
SC model	0.6	5.18	7.82	0.2	2.0	8.9	0.4	23.0	51.8
					3.0	13.4		8.0	18.0

charge will be considered in Section 4.4 below). The fitted values are given in Table 2. The SC and UP models provide close values for

capacitance C_s, and the corresponding C_d curves are in good agreement with the experimental data. The SC model provides larger variation of C_d in comparison with the UP model. In Table 2, we also present the properties of inner and outer parts of the Stern layer for two values of inner permittivity ($\varepsilon_i = 2$ and $\varepsilon_i = 3$). Once this property and δ_i, δ_o, C_s are specified, the capacitances C_i, C_o and permittivity ε_o can be determined from (9) and (10). The obtained capacitances lie in the range typical for metal/electrolyte interfaces [48,49]. Note that the values of ε_i are taken only as examples and cannot be determined from the experimental data available in this study.

The surface charge density calculated on the basis of fitted C_s values is in excellent agreement with the experimental results, see Fig. 6 (b). The diffuse layer potential is presented in Fig. 6 (c). According to the SC model, a significant potential drop occurs within the Stern layer. The magnitude of diffuse layer potential provided by the UP model is around two times smaller than that determined

from the SC model. In what follows, the fitted values of C_s will be employed in analyzing the experimental data on ionic selectivity of C–Nafen membrane.

4.4. Switchable ionic selectivity of C–Nafen membrane

In this section, the ionic selectivity of membrane is investigated by measuring the membrane potential at zero current with different applied surface potentials. Its sing and magnitude are compared with those corresponding to ideal cation or anion selective membranes.

A typical evolution of membrane potential with time during experimental runs is presented in Fig. 7. First, the membrane potential is measured for equal electrolyte concentrations in both reservoirs (in the considered example, $C_L = C_R = 1$ mM). The measurement starts when the external potential is not applied, and the measured value is close to zero as expected. Then a series of applied potentials from +600 mV to −600 mV with the step of 100 mV is applied consecutively to the membrane (this period starts at time moment $t = 0$ min). The measurement shows some deviation
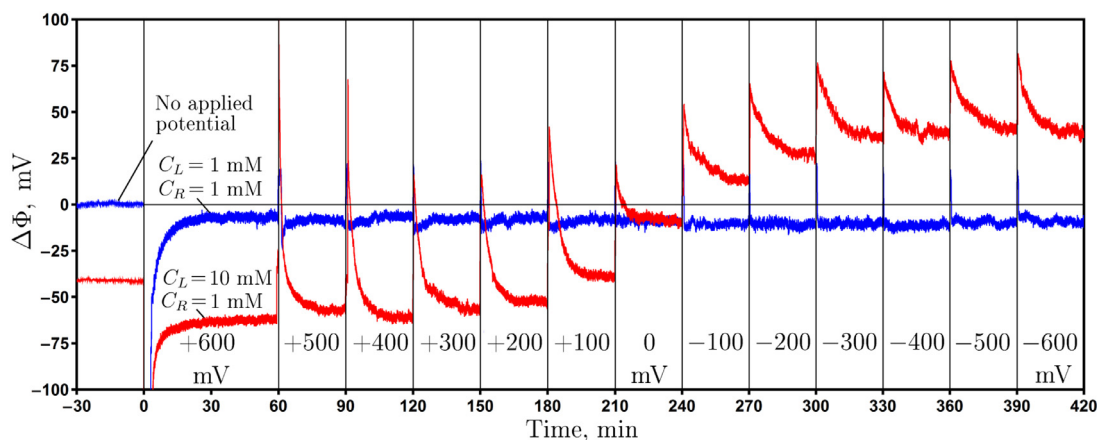
Fig. 7. The temporal evolution of membrane potential at different surface potentials for equal and different KCl concentrations in the reservoirs.
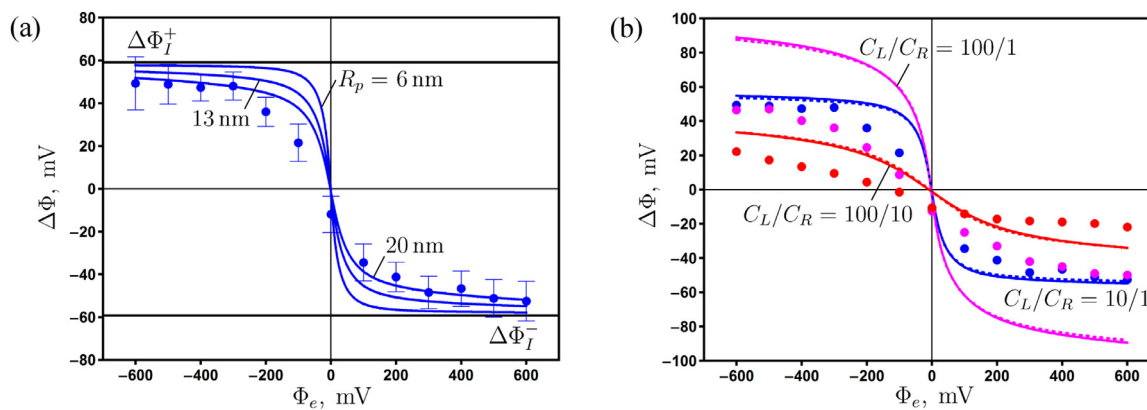

Fig. 8. The membrane potential vs applied surface potential for different pore radii (a) and different KCl concentrations in the reservoirs (b). Experiment (circles), calculations by the UP model using ion concentrations (solid curves) and activities (dashed curves).

of membrane potential from the expected zero value (about 6–12 mV). It can be explained by the presence of small residual current between the membrane and counter–electrode operated by the Potentiostat B, see the scheme of experimental setup in Fig. 3 (a) and current evolution with time in Fig. 5. This residual current affects the potential difference measurement by the two electrodes connected to Potentiostat A. This explanation is in line with the theoretical study of interaction between a switchable nanopore electrode and two reference electrodes in the reservoirs separated by the nanopore [67].

When the concentrations in the reservoirs are different ($C_L = 10$ mM and $C_R = 1$ mM) and surface potential is not applied externally, the measured membrane potential is -34 mV. It corresponds to moderate anion selectivity (for ideal anion selectivity, formula (1) provides $\Delta\Phi_I^- = -59.2$ mV). The variation of applied potential from positive (+600 mV) to negative (- 600 mV) values essentially affects the membrane potential. At each step, the equilibrium is established in around 15 min, which agrees well with the membrane charging time, see Fig. 5. The value of membrane potential is determined by time averaging of the measured signal after reaching the plateau. At each applied potential, the membrane potential measured at different reservoir concentrations is corrected by subtracting the value corresponding to equal reservoir concentrations. The change of membrane potential from negative to positive values when the applied potential varies from positive to negative values confirms the switch of ionic selectivity from anion to cation.

It should be noted that a relatively large charging time (15 min) is explained by the large membrane thickness of 400 μm. The decrease of thickness would provide a significant reduction of

charging time (e.g. by making a selective layer of carbon coated nanofibers with thickness of a few μm on top of a macroporous support). Note that the characteristic time of ion diffusion through a membrane is proportional to the square of its thickness.

Fig. 8 (a) shows the dependence of membrane potential on the surface potential. The data of 6 experiments with different samples are processed to calculate the mean values and standard deviations. The solid curves correspond to the theoretical predictions for pore radii of 6, 13, 20 nm (the pore size mean value plus/minus its standard deviation according to Table 1). The chemical charge and the boundary layer thickness are taken to be zero in the calculations. One can see that the curve corresponding to the largest pore radius (20 nm) is close the experimental results, but still does not fully agree with them. In addition, the experimental dependence does not cross the origin being slightly shifted in the negative potential direction. Fig. 8 (b) shows the results for different electrolyte concentrations in the reservoirs. The change of membrane potential magnitude in comparison with the case $C_L/C_R = 10/1$ is related to the increase of concentration ratio (case $C_L/C_R = 100/1$) or to the decrease of Debye length (case $C_L/C_R = 100/10$). However, the calculations provide larger variation of membrane potential magnitude in comparison with the experiment, especially for the case $C_L/C_R = 100/1$. The use of activities instead of concentrations or the SC model instead of UP model has a minor effect on the obtained results.

We have performed a simultaneous fit of three experimental data sets shown in Fig. 8 (b) by the SC and UP models using the effective chemical charge density Σ_c' and boundary layer thickness L_b as fitting parameters. The obtained results demonstrate a very
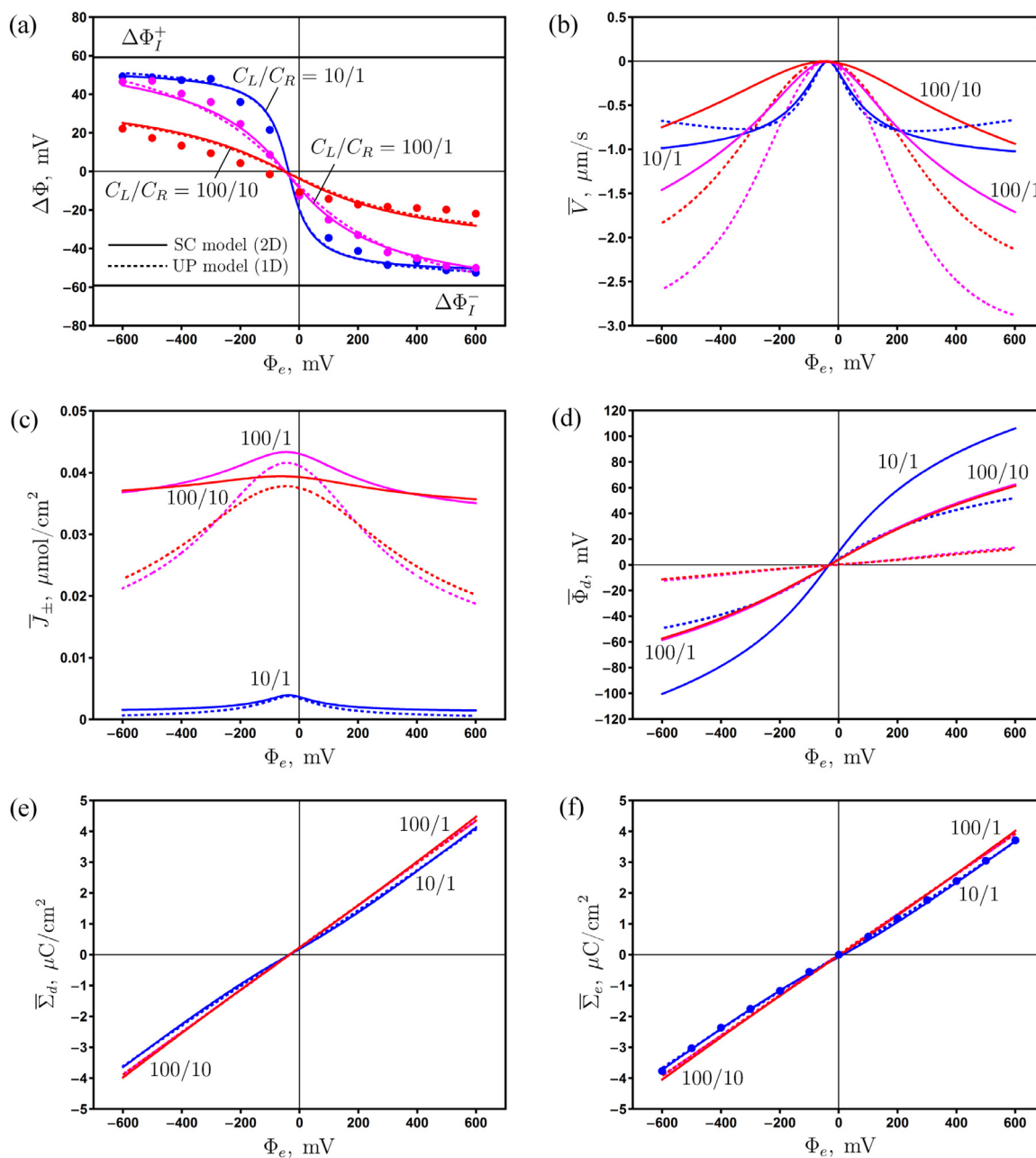
Fig. 9. The membrane potential (a), average axial velocity (b), average ion fluxes (c), average diffuse layer potential (d), average charge density at the oHp (e), and average surface charge density (f) vs the applied surface potential for different KCl concentrations in the reservoirs. Experiment (circles), calculations by the SC model (solid curves) and UP model (dashed curves).

Table 3
The values of fitted parameters.

Model	L_b μm	Σ_c' μC/cm^2	Σ_c μC/cm^2	$\Phi_{\overline{\Sigma}_d=0}$ mV
UP model	57.6	0.235	0.298	−34
SC model	42.5	0.265	0.302	−34

good agreement with the experimental data, see Fig. 9 (a). The values of fitted parameters are presented in Table 3. The SC model provides lower boundary layer thickness due to higher ion fluxes in comparison with the UP model, see Fig. 9 (c). The fitted chemical charge density is positive, so the zero average diffuse charge corresponds to the negative surface potential of −34 mV (Fig. 9 (e)). Note that the values of chemical charge density Σ_c in Table 3 are

recovered from formulas (7) and (9), where the capacitance C_i corresponds to the relative permittivity $\varepsilon_i = 2$.

At the surface potential of −34 mV, the membrane becomes non–selective, which results in the maximum value of ion fluxes and vanishing of solution flow (Fig. 9 (b) and (c)). The increase of surface potential magnitude introduces ionic selectivity, which leads to the development of (electro) osmotic flow and the decrease of ion fluxes due to co–ion exclusion in the pore. The ions are transported from the reservoir L with higher salt concentration to the reservoir R with lower concentration, while the osmotic flow occurs in opposite direction. Note that the ion fluxes become larger when the concentrations C_L and C_R as well as their ratio are increased. The calculated surface charge density shows a weak dependence on electrolyte concentration (Fig. 9 (f)) and agrees very well with the experimental values determined from charging cur-
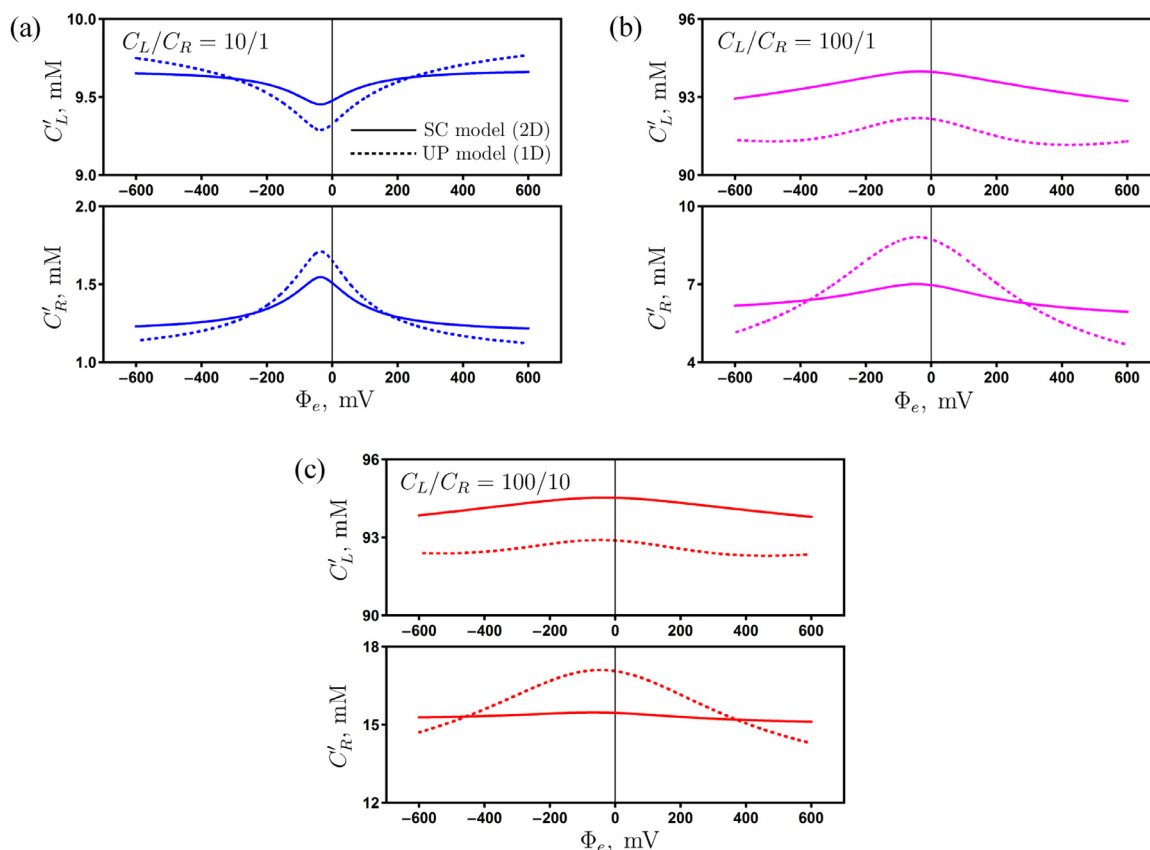
Fig. 10. The concentrations near the membrane surface for $C_L/C_R = 10/1$ (a), $C_L/C_R = 100/1$ (b), and $C_L/C_R = 100/10$ (c) vs. the applied surface potential.

rent evolution, see Fig. 5. The magnitude of diffuse layer potential significantly decreases with increasing the electrolyte concentration (Fig. 9 (d)) due to more effective screening of surface charge at higher salt concentrations.

The concentrations near the membrane surface are presented in Fig. 10. The presence of boundary layers leads to the increase (decrease) of concentration in the reservoir with lower (higher) salt concentration. The effect is most pronounced when the membrane is non–selective ($\Phi_e = -34$ mV) due to the maximum of ion fluxes. The SC model predicts a weaker effect of boundary layers in comparison with the UP model due to smaller fitted thickness of the layers (see Table 3), but at high applied potentials the situation is the opposite (especially at low concentration side) since the ion fluxes calculated by the SC model become much higher (see Fig. 9 (c)).

We can conclude that the SC and UP models provide close results for membrane potential, surface charge, and diffuse layer charge densities. The UP model overestimates the solution velocity and ion concentrations at the membrane surface, while it underestimates the ion fluxes and diffuse layer potential.

5. Conclusion

We have developed the theoretical framework for describing ion transport in nanoporous membranes with electrically conductive surface. The classical Space charge and Uniform potential models for constant surface charge are first extended to the case of constant surface potential taking into account the Stern layer and the presence of chemical charge. The theory of amphifunctional interfaces is generalized to cylindrical nanopores, where ions are transported by convection, diffusion, and electromigration. A new robust and computationally efficient method for solving the model equations is proposed.

The developed models are verified experimentally using C–Nafen membranes prepared from alumina nanofibers with conductive carbon coating. The membranes have the average pore size of of 13±7 nm and high porosity of 65 %. The cyclic voltammetry shows that the C–Nafen membrane behaviour is close to an ideally polarized electrode in the potential range from - 600 to +600 mV with respect to 4.2 Ag/AgCl electrode. The potentiostatic charging is used to determine the dependence of surface charge density and differential capacitance on the applied potential. The latter is fitted by the models to determine the Stern layer capacitance (7.04 and 7.82 μF/cm^2 for the UP and SC models, respectively).

The ionic selectivity is investigated by measuring the membrane potential at zero current when a membrane separates two KCl aqueous solutions of different concentrations. It is shown that the variation of surface potential from +600 to - 600 mV results in a continuous change of selectivity from anion to cation. The experimental data for different concentration ratios are simultaneously fitted by the UP and SC models using the chemical charge density and concentration boundary layer thickness as fitting parameters. The determined thicknesses are 57.6 μm and 42.5 μm for the UP and SC models, respectively, while the corresponding chemical charge densities are 0.235 and 0.265 μC/cm^2. The potential, at which the average diffuse layer charge is zero, is determined to be - 34 mV. At this point, the membrane becomes non–selective, which results in the maximum value of ion fluxes and vanishing of osmotic flow. At high applied potentials, the decrease of ion fluxes and rise of osmotic flow velocity are observed. The SC and UP models provide close results for membrane potential and surface charge density, and demonstrate a good agreement with the experimental data. The UP model overestimates the solution velocity

and ion concentrations at the membrane surface, while it underestimates the ion fluxes and diffuse layer potential in comparison with the SC model.

The obtained results provide new insights into the theoretical and experimental understanding of ion transport in stimuli–responsive membranes operated by the electric field. The potential applications include electric–field assisted nanofiltration, (reverse) electrodialysis, electrochemical sensors, and nanofluidic devices.

Declaration of Competing Interest

No conflict of interest is declared for manuscript Switchable ionic selectivity in membranes with electrically conductive surface: theory and experiment

Credit authorship contribution statement

Ilya I. Ryzhkov: Conceptualization, Methodology, Writing - original draft, Writing - review & editing, Supervision. **Margarita A. Shchurkina:** Investigation, Formal analysis. **Elena V. Mikhlina:** Investigation, Methodology. **Mikhail M. Simunin:** Formal analysis, Resources. **Ivan V. Nemtsev:** Investigation.

Acknowledgement

Supplementary material

Supplementary material associated with this article can be found, in the online version, at 10.1016/j.electacta.2021.137970

References

[1] L. Y. Chu, Smart Membrane Materials and Systems, Springer–Verlag, Berlin, 2011.
[2] D. Wandera, S.R. Wickramasinghe, S.M. Husson, Stimuli–responsive membranes, J. Membr. Sci. 357 (2010) 6–35.
[3] Z. Liu, W. Wang, R. Xie, X.J. Ju, L.Y. Chu, Stimuli–responsive smart gating membranes, Chem. Soc. Rev. 45 (2016) 460–475.
[4] L.A. Baker, P. Jin, C.R. Martin, Biomaterials and biotechnologies based on nanotube membranes, Crit. Rev. Solid State Mater. Sci. 30 (2005) 183–205.
[5] P.Y. Apel, O.V. Bobreshova, A.V. Volkov, V.V. Volkov, V.V. Nikonenko, I.A. Stenina, A.N. Filippov, Y.P. Yampolskii, A.B. Yaroslavtsev, Prospects of membrane science development, Membr. Membr. Technol. 1 (2) (2019) 45–63.
[6] R. Ghosh, Stimuli–responsive membranes for separations, in Polymers and Polymeric Composites: AReference Series, Springer, 2019. 491–508
[7] S.C. Low, Q.H. Ng, Progress of stimuli responsive membranes in water treatment, in: Advanced Nanomaterials for Membrane Synthesis and Its Applications, 2019, pp. 69–99.
[8] A. Gulzar, S. Gai, P. Yang, C. Li, M.B. Ansari, J. Lin, Stimuli responsive drug delivery application of polymer and silica in biomedicine, J. Mater. Chem. B 3 (44) (2015) 8599–8622.
[9] A. Gugliuzza, Smart Membranes and Sensors: Synthesis, Characterization, and Applications, Scrivener Publishing & Whiley, 2014.
[10] X. Hou, W. Guo, L. Jiang, Biomimetic smart nanopores and nanochannels, Chem. Soc. Rev 40 (2011) 2385–2401.
[11] M. Tagliazucchi, I. Szleifer, Transport mechanisms in nanopores and nanochannels: can we mimic nature? Mater. Today 18 (2015) 131–142.
[12] Z.S. Siwy, S. Howorka, Engineered voltage–responsive nanopores, chem, Soc. Rev 39 (2010) 1115–1132.
[13] R.B. Schoch, J. Han, P. Renaud, Transport phenomena in nanofluidics, Rev. Modern Phys 80 (2008) 839–883.
[14] M. Nishizawa, V.P. Menon, C.R. Martin, Metal nanotubule membranes with electrochemically switchable ion–transport selectivity, Science 268 (1995) 700–702.
[15] C.R. Martin, M. Nishizawa, K. Jirage, M. Kang, S.B. Lee, Controlling ion–transport selectivity in gold nanotubule membranes, Adv. Mater 13 (2001) 1351–1362.
[16] M.S. Kang, C.R. Martin, Investigations of potential–dependent fluxes of ionic permeates in gold nanotubule membranes prepared via the template method, Langmuir 17 (2001) 2753–2759.

[17] S.P. Surwade, S.H. Chai, J.P. Choi, X. Wang, J.S. Lee, I.V. Vlassiouk, S.M. Mahurin, S. Dai, Electrochemical control of ion transport through a mesoporous carbon membrane, Langmuir 30 (2014) 3606–3611.
[18] C. Cheng, G. Jiang, G.P. Simon, J.Z. Liu, D. Li, Low–voltage electrostatic modulation of ion diffusion through layered graphene–based nanoporous membranes, Nat. Nanotechnol. 13 (2018) 685–690.
[19] W. Guan, M.A. Reed, Electric field modulation of the membrane potential in solid–state ion channels, Nano Lett. 12 (2012) 6441–6447.
[20] W. Guan, R. Fan, M.A. Reed, Field–effect reconfigurable nanofluidic ionic diodes, Nat. Commun 2 (2011). Article no. 506
[21] Q. Wang, C.S. Cha, J. Lu, L. Zhuang, Ionic conductivity of pure water in charged porous nitride, ChemPhysChem 13 (2012) 514–519.
[22] P. Gao, C.R. Martin, Voltage charging enhances ionic conductivity in gold nanotube membranes, ACS Nano 8 (2014) 8266–8272.
[23] D.A. McCurry, R.C. Bailey, Nanoporous gold membranes as robust constructs for selectively tunable chemical transport, J. Phys. Chem. C 120 (2016) 20929–20935.
[24] H. Zhang, X. Quan, X. Fan, C. Yi, S. Chen, H. Yu, Y. Chen, Improving ion rejection of conductive nanofiltration membrane through electrically enhanced surface charge density, Environ. Sci. Technol. 53 (2019) 868–877.
[25] J. Sun, C. Hu, B. Wu, H. Liu, J. Qu, Improving ion rejection of graphene oxide conductive membranes by applying electric field, J. Membr. Sci. 604 (2020) 118077.
[26] P. Ramírez, S. Mafé, A. Alcaraz, J. Cervera, Modeling of ph-switchable ion transport and selectivity in nanopore membranes with fixed charges, J. Phys. Chem. B 107 (2003) 13178–13187.
[27] J.R. Ku, S.M. Lai, N. Ileri, P. Ramírez, S. Mafe, P. Stroeve, ph and ionic strength effects on amino acid transport through au–nanotubule membranes charged with self–assembled monolayers, J. Phys. Chem. C 111 (2007) 2965–2973.
[28] C. Amatore, A.I. Oleinick, I. Svir, Theory of ion transport in electrochemically switchable nanoporous metallized membranes, ChemPhysChem 10 (2009) 211–221.
[29] Z. Ni, H. Qiu, W. Guo, Electrically tunable ion selectivity of charged nanopores, J. Phys. Chem. C 122 (2018) 29380–29385.
[30] R.J. Gross, J.F. Osterle, Membrane transport characteristics of ultrafine capillaries, J. Chem. Phys. 49 (1968) 228–234.
[31] E.H. Cwirko, R.G. Carbonell, Transport of electrolytes in charged pores: analysis using the method of spatial averaging, J. Colloid Interface Sci. 129 (1989) 513–531.
[32] P.B. Peters, R. van Roij, M.Z. Bazant, P.M. Biesheuvel, Analysis of electrolyte transport through charged nanopores, Phys. Rev. E 93 (2016) 053108.
[33] J. Catalano, P.M. Biesheuvel, AC–driven electro–osmotic flow in charged nanopores, Eur. Phys. Lett. 123 (2018) 58006.
[34] A. Szymczyk, B. Aoubiza, P. Fievet, J. Pagetti, Electrokinetic phenomena in homogeneous cylindrical pores, J. Colloid Interface Sci. 216 (1999) 285–296.
[35] P. Fievet, A. Szymczyk, C. Labbez, B. Aoubiza, C. Simon, A. Foissy, J. Pagetti, Determining the zeta potential of porous membranes using electrolyte conductivity inside pores, J. Colloid Interface Sci. 235 (2001) 383–390.
[36] I. Makra, G. Jágerszki, I. Bitter, R.E. Gyurcsányi, Nernst–planck/poisson model for the potential response of permselective gold nanopores, Electrochim. Acta 73 (2012) 70–77.
[37] M.B. Kristensen, A. Bentien, M. Tedesco, J. Catalano, Counter–ion transport number and membrane potential in working membrane systems, J. Colloid Interface Sci. 504 (2017) 800–813.
[38] J. Catalano, H.V.M. Hamelers, A. Bentien, P.M. Biesheuvel, Revisiting Morrison and Osterle 1965: the efficiency of membrane–based electrokinetic energy conversion, J. Phys. 28 (2016) 324001.
[39] I.I. Ryzhkov, D.V. Lebedev, V.S. Solodovnichenko, A.V. Shiverskiy, M.M. Simunin, Induced-charge enhancement of diffusion potential in membranes with polarizable nanopores, Phys. Rev. Lett. 119 (2017) 226001.
[40] I.I. Ryzhkov, A.V. Minakov, Theoretical study of electrolyte transport in nanofiltration membranes with constant surface potential/charge density, J. Membr. Sci. 520 (2016) 515–528.
[41] M.Z. Bazant, T.M. Squires, Induced–charge electrokinetic phenomena, Curr. Opin. Colloid Interface Sci. 15 (2010) 203–213.
[42] J. Fuhrmann, C. Guhlke, A. Linke, C. Merdon, R. Müller, Induced charge electroosmotic flow with finite ion size and solvation effects, Electrochim. Acta 317 (2019) 778–785.
[43] I.I. Ryzhkov, D.V. Lebedev, V.S. Solodovnichenko, A.V. Minakov, M.M. Simunin, On the origin of membrane potential in membranes with polarizable nanopores, J. Membr. Sci. 549 (2018) 616–630.
[44] I.I. Ryzhkov, A.S. Vyatkin, A.V. Minakov, Theoretical study of electrolyte diffusion through polarizable nanopores, J. Siber. Fed. Univ. 11 (4) (2018) 494–504.
[45] I.I. Ryzhkov, A.S. Vyatkin, M.I. Medvedeva, Modelling of electrochemically switchable ion transport in nanoporous membranes with conductive surface, J. Siber. Fed. Univ. 12 (5) (2019) 579–589.
[46] I.I. Ryzhkov, A.S. Vyatkin, E.V. Mikhlina, Modelling of conductive nanoporous membranes with switchable ionic selectivity, Membr. Membr. Technol. 2 (1) (2020) 10–19.
[47] L. Zhang, P.M. Biesheuvel, I.I. Ryzhkov, Theory of ion and water transport in electron–conducting membrane pores with ph–dependent chemical charge, Phys. Rev. Appl. 12 (2019) 014039.
[48] J. Duval, J. Lyklema, J.M. Kleijn, H.P.V. Leeuwen, Amphifunctionally electrified interfaces: coupling of electronic and ionic surface–charging processes, Langmuir 17 (2001) 7573–7581.

[49] J. Duval, M.J. Kleijn, J. Lyklema, H.P.V. Leeuwen, Double layers at amphifunctionally electrified interfaces in the presence of electrolytes containing specifically adsorbing ions, J. Electroanal. Chem. 532 (2002) 337–352.

[50] J. Huang, J. Zhang, M. Eikerling, Theory of electrostatic phenomena in water–filled pt nanopores, Faraday Discuss. 193 (2016) 427–446.

[51] J. Huang, A. Malek, J. Zhang, M.H. Eikerling, Non–monotonic surface charging behavior of platinum: a paradigm change, J. Phys. Chem. C 120 (2016) 13587–13595.

[52] J. Huang, T. Zhou, J. Zhang, M. Eikerling, Double layer of platinum electrodes: Non–monotonic surface charging phenomena and negative double layer capacitance, J. Chem. Phys. 148 (2018) 044704.

[53] D.V. Lebedev, A.V. Shiverskiy, M.M. Simunin, V.S. Solodovnichenko, V.A. Parfenov, V.V. Bykanova, S.V. Khartov, I.I. Ryzhkov, Preparation and ionic selectivity of carbon–coated alumina nanofiber membranes, Petrol. Chem. 57 (4) (2017) 306–317.

[54] V.S. Solodovnichenko, D.V. Lebedev, V.V. Bykanova, A.V. Shiverskiy, M.M. Simunin, V.A. Parfenov, I.I. Ryzhkov, Carbon coated alumina nanofiber membrane for selective ion transport, Adv. Eng. Mater. 20 (2017) 1700244.

[55] D.V. Lebedev, V.S. Solodovnichenko, M.M. Simunin, I.I. Ryzhkov, The influence of electric field on the ion transport on nanoporous membranes with conductive surface, Petrol. Chem. 58 (6) (2018) 474–481.

[56] Y. Tanaka, Ion Exchange Membranes: Fundamentals and Applications, Elsevier, Amsterdam, 2015.

[57] P.H. Barry, J.M. Diamond, Effect of unstirred layers on membrane phenomena, Physiol. Rev. 64 (3) (1984) 763–872.

[58] T.J. Pedley, Calculation of the unstirred layer thickness in membrane transport experiments: a survey, Q. Rev. Biophys. 16 (2) (1983) 115–150.

[59] C.H. Hamann, A. Hamnett, W. Veilstich, Electrochemistry, Wiley–VCH, Wienheim, 2007.

[60] P.M. Biesheuvel, J.E. Dykstra, Physics of electrochemical processes. http://www.physicsofelectrochemicalprocesses.com.

[61] M.A. Brown, Z. Abbas, A. Kleibert, R.G. Green, A. Goel, S. May, T.M. Squires, Determination of surface potential and electrical double–layer structure at the aqueous electrolyte–nanoparticle interface, Phys. Rev. X 6 (2016) 011007.

[62] G. Trefalt, S.H. Behrens, M. Borkovec, Charge regulation in the electrical double layer: ion adsorption and surface interactions, Langmuir 32 (2016) 380–400.

[63] H. Wang, J. Fang, L. Pilon, Scaling laws for carbon–based electric double layer capacitors, Electrochim. Acta 109 (2013) 316–321.

[64] Nafen alumina nanofibers. http://www.anftechnology.com/nafen/.

[65] V.S. Solodovnichenko, M.M. Simunin, D.V. Lebedev, A.S. Voronin, A.V. Emelianov, Y.L. Mikhlin, V.A. Parfenov, I.I. Ryzhkov, Coupled thermal analysis of carbon layers deposited on alumina nanofibres, Thermochim. Acta 675 (2019) 164–171.

[66] A.J. Bard, L.R. Faulkner, Electrochemical methods, Fundamentals and Applications, John Wiley & Sons, New York, 2001.

[67] T. Albrecht, How to understand and interpret current flow in nanopore/electrode devices, ACS Nano 5 (8) (2011) 6714–6725.